

7 Urban Micrometeorology

7.1 Introduction

Having examined the urban fine aerosol flux measurements made above the City of Edinburgh in chapter six, this section focuses on aspects of urban micrometeorology relevant to pollutant and heat transport. The purpose of this chapter is to present results supporting the findings of chapter six, rather than to provide a full review of urban micrometeorology or to develop further generalised results.

7.1.1 Background

Investigations of urban micrometeorology are comparatively well represented in the literature, with comprehensive treatments of the urban heat balance, city scale aerodynamic (*e.g.* Feigenwinter *et. al.*, 1999) and roughness behaviour (*e.g.* Grimmond and Oke, 1999; Grimmond *et. al.*, 1998) and the so-called urban heat island effect (*e.g.* Grimmond and Oke, 1998) available. Recently much attention has also been devoted to the study of airflow through urban canyon systems, with a view to understanding the behaviour of pollutants on the scale of individual streets and to elucidate the mechanism by which pollutants are removed from the immediate vicinity of sources (*e.g.* Barlow and Belcher, 2002).

7.1.2 Investigations of the Urban Heat Balance

While there have been attempts to extend our existing knowledge of turbulent spectral and co-spectral behaviour to the boundary layers of cities (notably by Roth and Oke, 1993), more published data are required before an assessment can be made of the specific effects of urban surfaces on the structure of turbulence. To date, studies have exclusively used parameterisations for crop surfaces (*e.g.* Panofsky and Dutton, 1984; Wyngaard and Coté, 1972). Presumably the use of full range spectral models with

higher roughness lengths would give rise to larger “peak frequencies”, however there are no examples of the application of full range spectral models (e.g. Kaimal *et. al.*, 1972) to urban surfaces in the literature.

The following sections include experimental results from above the City of Edinburgh gained from the UMIST CPC flux system. These serve to elucidate the mechanisms of aerosol and heat transport above the study city. Details of the experimental arrangement are given in chapters three and six.

7.2 Urban Heat Balance

As for any surface, the net energy input to an urban area must be equalled by energy loss. In the case of cities, there is an extra term in the energy balance not present for natural or semi-natural surfaces. Along with incoming short wave radiation, anthropogenic heat input must also be considered. In terms of direct energy balance measurements, this additional energy manifests itself as an increase in latent and sensible heat fluxes and a decrease in net radiation (R_n). The decrease in net radiation is due to increased upward long wave emission, – according to the Stephan-Boltzmann law an increase of 1 °C in surface temperature (assuming black body emissivity) results in an increase in R_{Lu} of 5 – 6 W m⁻². However, determination of the anthropogenic energy input from estimates of the deficit in R_n is complicated by the fact that the polluted urban boundary layer also gives rise to an increase in downward long wave flux (R_{Ld}). The energy balance can be expressed as:

$$R_n + E_{ff} + E_{nff} = \lambda E + H \quad (7.1)$$

where E_{ff} and E_{nff} are the fossil fuel and non-fossil fuel derived components of the anthropogenic energy input respectively, and $R_n = S_t + R_{Ld} - R_{Lu}$ with S_t being the (global) incident short wave radiation. This simplified expression for the urban energy balance assumes integration over a significant time period (ideally at least one full diurnal cycle) so that heat storage effects can be neglected.

Nemitz *et. al.* (2002 e) estimated that the total anthropogenic energy input was 44 W m^{-2} from an analysis of the energy balance of the study city, measured during the SASUA 3 campaign. The analysis is shown in figure 1. There are a number of interesting features in figure 1. The integrated sum of sensible and latent heat flux is larger than the

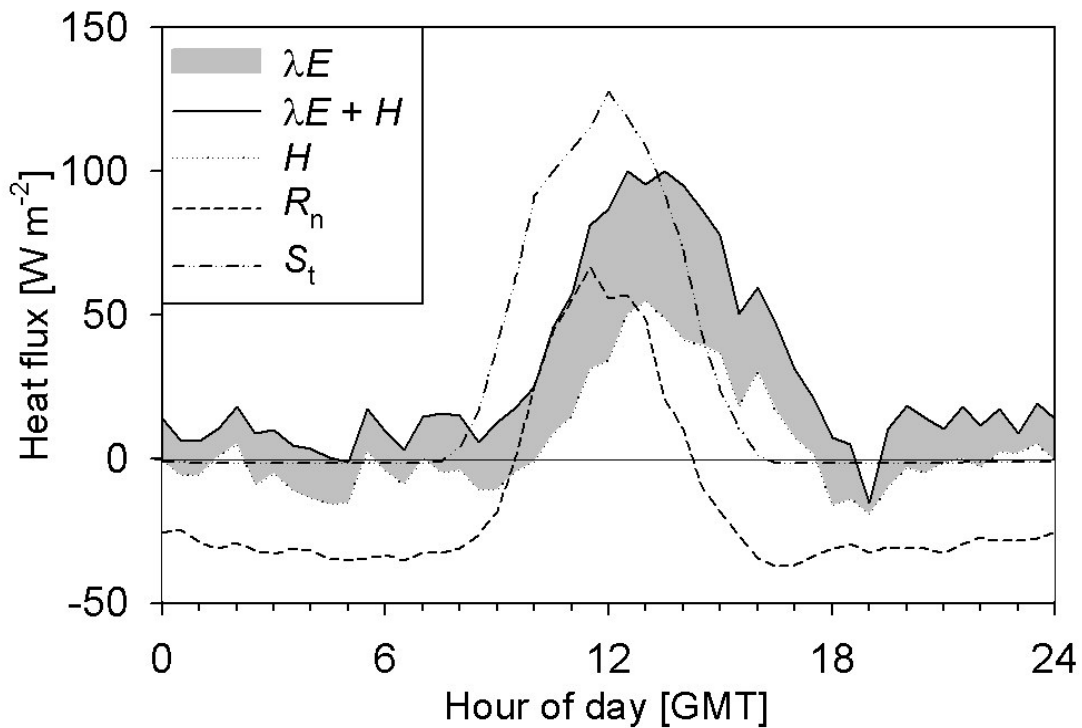


Figure 1. Diurnally averaged measured fluxes of sensible and latent heat fluxes, net radiation and solar radiation for Edinburgh city centre. From Nemitz *et. al.* (2002)

downward net radiation flux. This is accounted for by the additional 44 W m^{-2} noted above, – in fact this disparity is how the figure was calculated.

The turbulent heat fluxes are noticeably out of phase with the radiation fluxes. This is attributed to the combined effects of heat storage in the fabric of buildings and other man made surfaces, and the fact that the diurnal cycle of $E_f (= E_{ff} + E_{nff})$ is different to that of R_n (this was also noted in chapter six with respect to aerosol emission). The source of the latent heat flux is unclear, given the efficient drainage characteristics of cities. However, a possible source may, again, be anthropogenic activity. Several such activities produce water vapour (*e.g.* cooking, combustion), and it is difficult to see an

alternative source of nocturnal water vapour emission when sensible heat fluxes are either negligible or negative at night.

To a first approximation, the anthropogenic energy input can be subdivided into the two components mentioned above using the available measurements. During the third SASUA campaign, CO₂ fluxes were measured at the city centre site. Assuming that all of the measured CO₂ emission was due to fossil fuel combustion, that the fuels responsible for those emissions had a C – H ratio of 0.866 and that 45 MJ g⁻¹ was the average calorific value of the fuels, Nemitz *et. al.* (2002 e) show that approximately 30% of the anthropogenic heat input (E_f) is derived from fossil fuel combustion (E_{ff}).

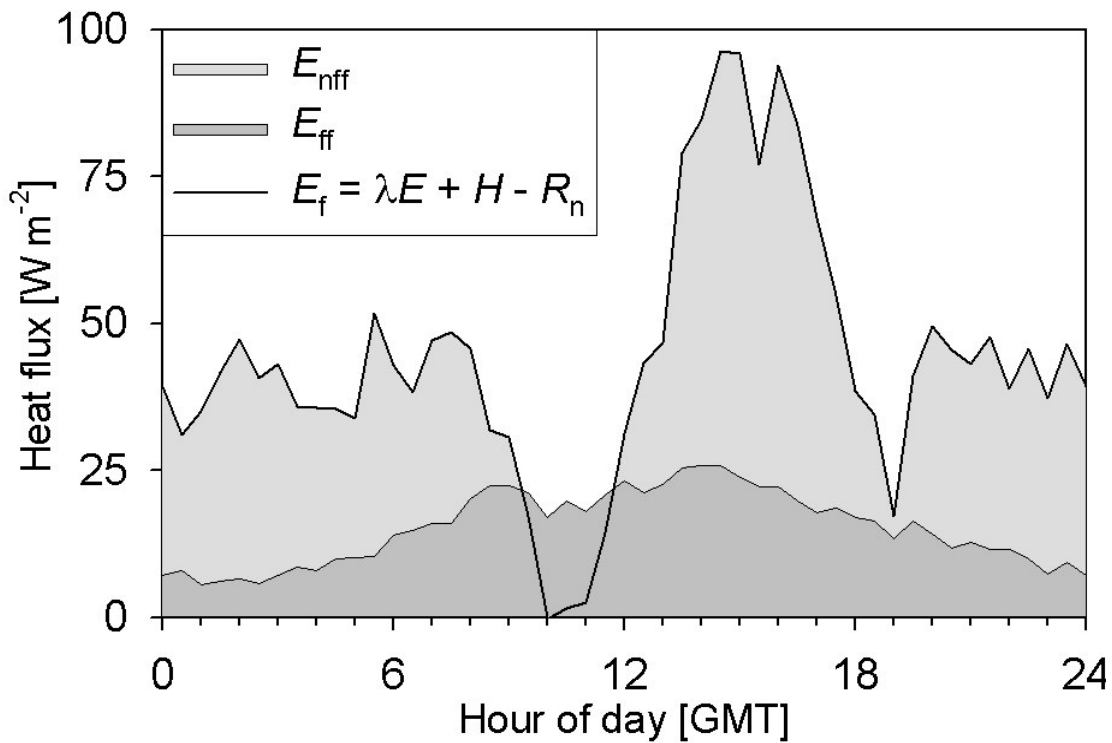


Figure 2. Diurnal average energy input from fossil fuels (derived from CO₂ flux measurements) and non-fossil fuel sources. From Nemitz *et. al.* (2002)

This calculation is shown in figure 2, where the E_f is explicitly derived from the net energy imbalance measured over the study city. Further sensible heat flux measurements are included in chapter six in support of the aerosol transport measurements. The following section introduces the spectral and co-spectral analyses of sensible heat and fine mode aerosol fluxes from the third urban measurement campaign.

7.3 Power Spectral Behaviour

Power spectra (as detailed in chapter two) of vertical wind velocity, air temperature and aerosol concentration are presented here as a means of assessing their respective variances in the urban boundary layer. The spectra are presented as three-dimensional plots of power spectrum (S_A) vs. stability parameter (ζ), in order to assess their variability under different stratifications. This style of presentation has not previously been used in the literature, but is an efficient means of gaining an impression of the stability dependence of scalar transport mechanisms. All power spectra in this section are normalised by the variance of the quantity in question. For further ease of comparison, the frequencies presented are non-dimensionalised as discussed in chapters two and four.

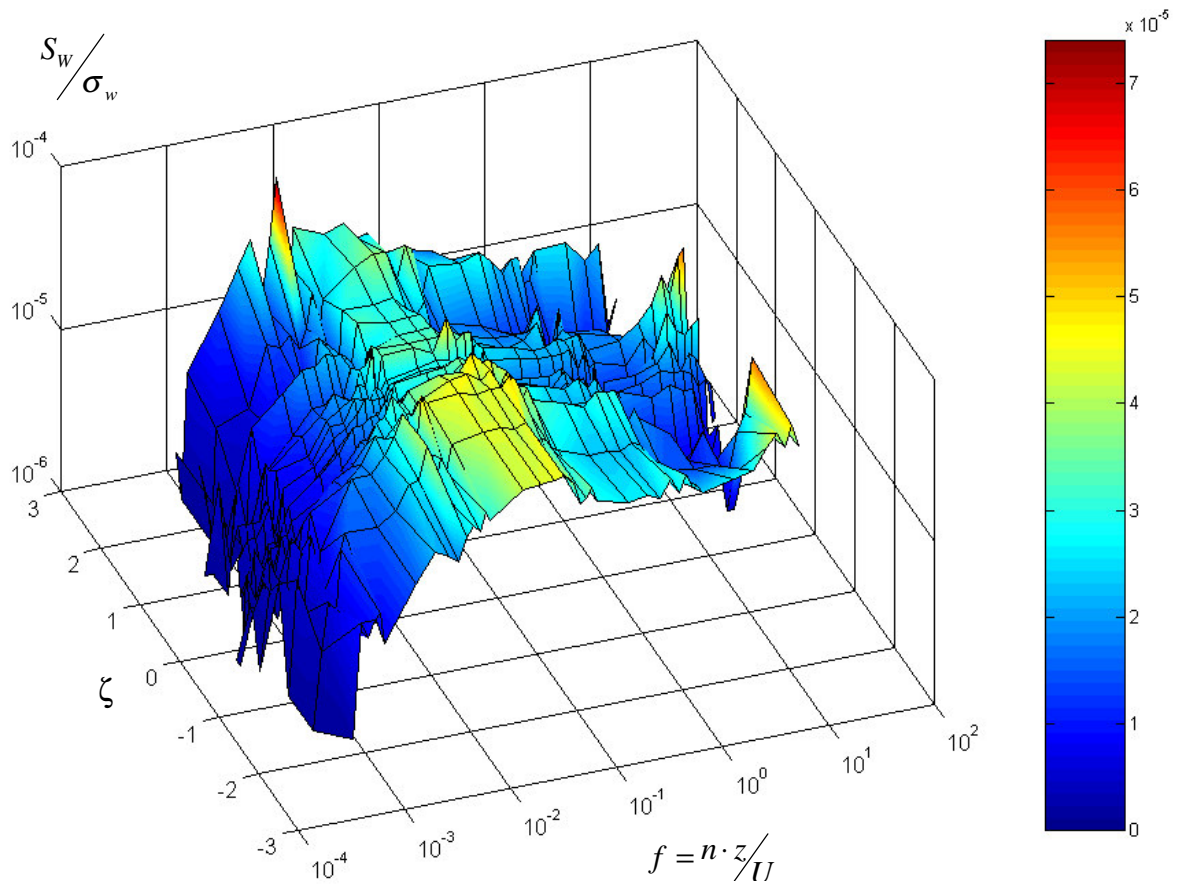


Figure 3. Vertical wind speed power spectrum vs. stability parameter from the third urban measurement campaign (SASUA 3).

7.3.1 Vertical Wind Speed

The range of vertical wind speed power spectra is displayed in figure 3. There is no large variation in the low frequency behaviour or peak frequency in these normalised spectra. With the exception of an outlying point in the most unstable category, the spectra behave as predicted (see section on spectral analysis in chapter 2). At high frequencies, the onset of white noise is determined by the atmospheric stability parameter. The characteristic positive gradient appears at the lowest frequencies in the neutral spectra. That this is apparent is a result of the normalisation of the power spectral density. The variance in the time series is comparatively low at all frequencies in the neutral boundary layer, and the un-normalised variance at which white noise appears is similar across the whole stability range.

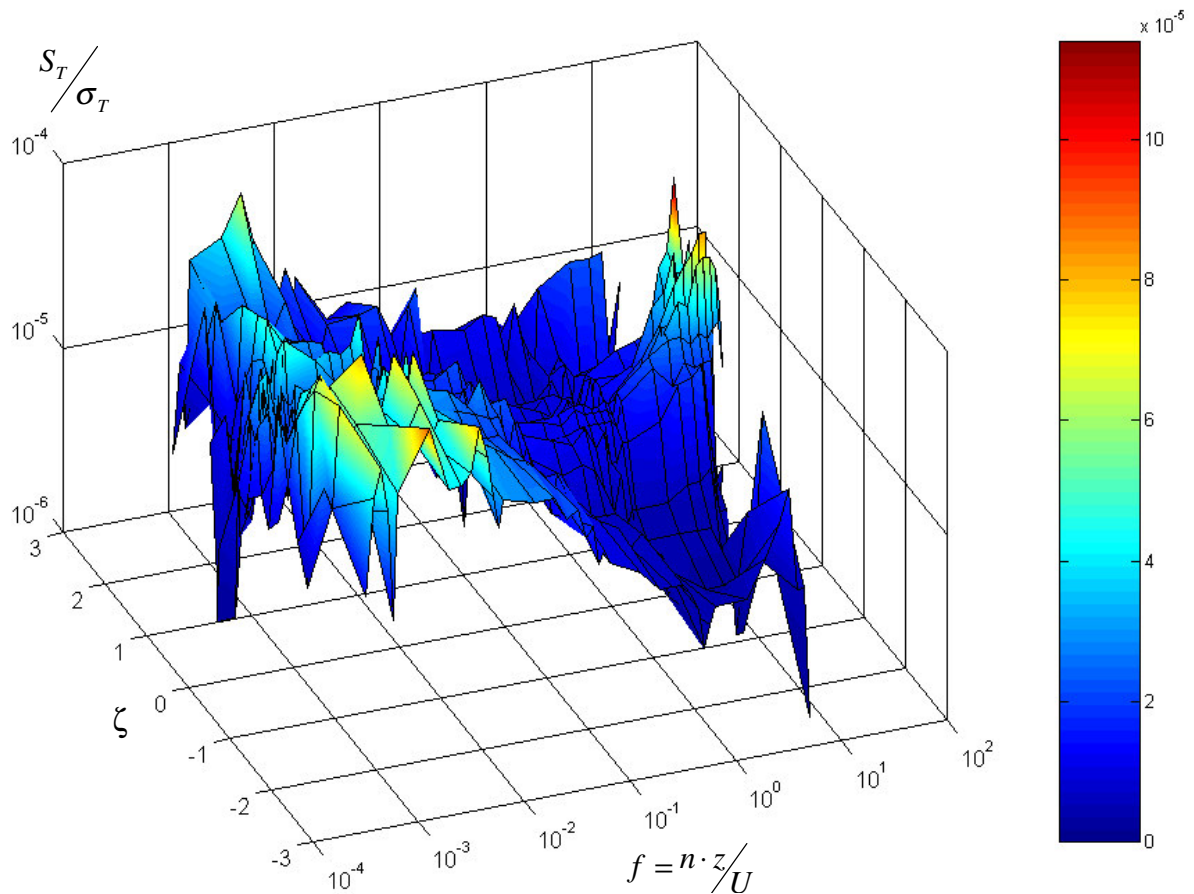


Figure 4. Vertical wind speed power spectrum vs. stability parameter from the third urban measurement campaign (SASUA 3).

7.3.2 Air Temperature

Figure 4 displays the power spectrum of virtual temperature measured by the ultrasonic anemometer. Similarly to the vertical wind speed power spectrum presented above, the white noise associated with the limit of the anemometer temperature resolution is first encountered around the neutral limit. This is associated with extremely low heat fluxes giving rise to very little “structure” in the time series of air temperature. As outlined above, the absolute values of the spectra around neutral stability are very low, and have been raised here by the spectral density normalisation used.

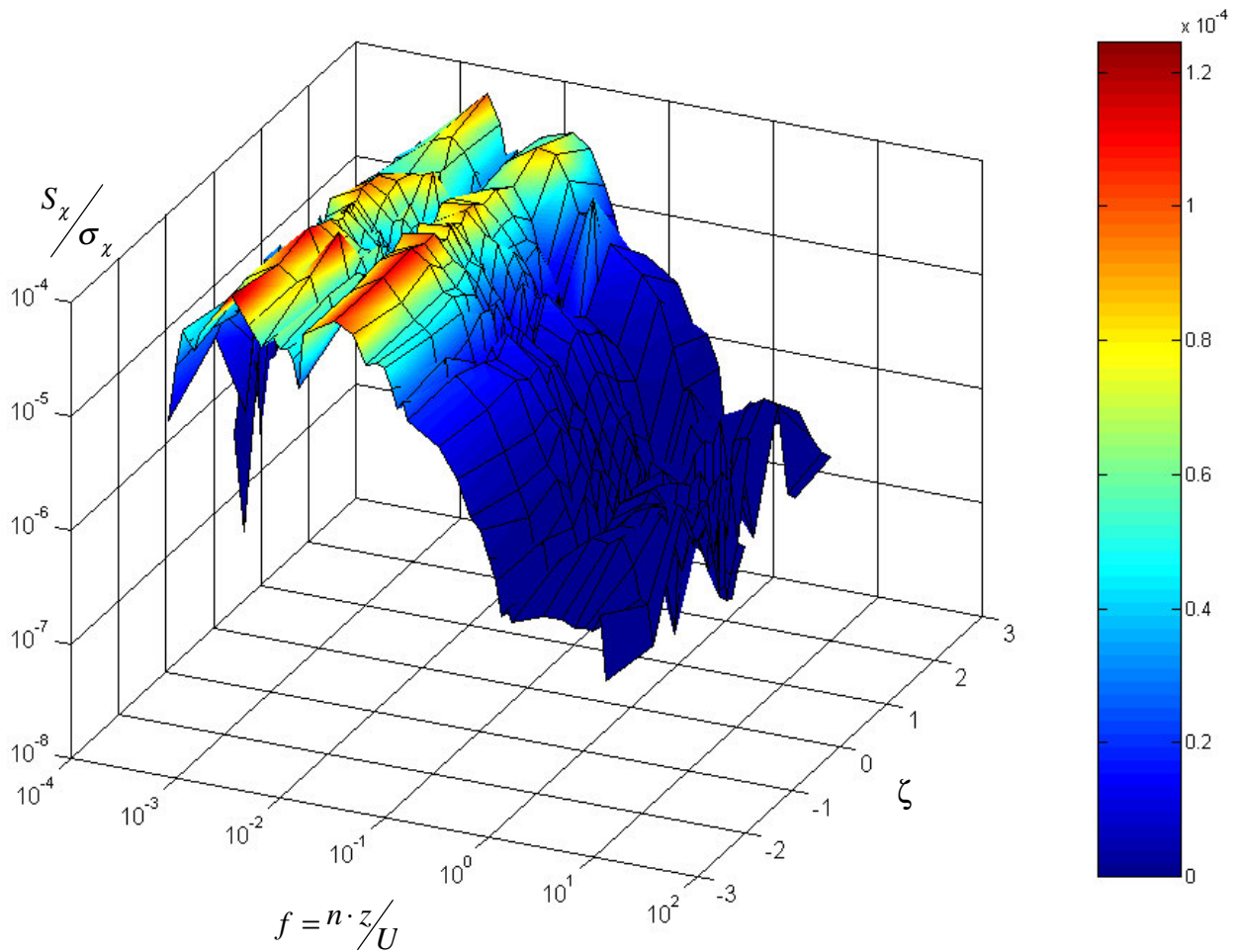


Figure 5. Fine mode aerosol concentration power spectrum vs. stability parameter from the third urban measurement campaign (SASUA 3).

7.3.3 Fine Aerosol Concentration

Figure 5 shows the final power spectrum to be examined. The frequency dependent behaviour of the aerosol time series appears to be uniform across the stability range. The onset of white noise appears in a similar location to that observed in the neutral wind speed power spectra across all values of ζ . The “fold” visible at around $f \sim 10^{-3}$ is not thought to be significant. It appears to be an artefact of the averaging process used for this set of power spectra. Examination of the co-spectrum of W and χ later will show that this is not correlated with vertical wind speed, and hence does not affect the measured aerosol flux.

7.4 Co-spectral Behaviour

7.4.1 Sensible Heat Flux

Plots of co-spectral density have been treated slightly differently to the power spectra in this section. The frequency non-dimensionalisation is the same as before, and all co-spectra have been normalised by their respective covariances. However, because co-spectra can take on negative values, the positive and negative values have been averaged separately to facilitate display of both “parts” of the spectra. Figure 6 shows the co-spectrum of temperature and vertical wind speed (C_{WT}). The positive part of C_{WT} – 6 (a) behaves similarly to the power spectra. The turn up to a positive gradient at high frequency in unstable conditions is thought to be a result of the flux not being fully resolved due to the combined limitations in resolution of the wind speed and temperature measurements. In these frequency-weighted plots, an increase in proportion to f^{+1} is equivalent to a constant covariance per unit frequency interval. This constant value corresponds to the lowest covariance calculable by the system. Interpretation of the “negative” portions of the co-spectra requires some comment here. Because the spectra are normalised by the co-variance of their constituent time series, the negative co-spectra represent transport *against the mean gradient* as determined by the measured flux, rather than simply upward or downward transport.

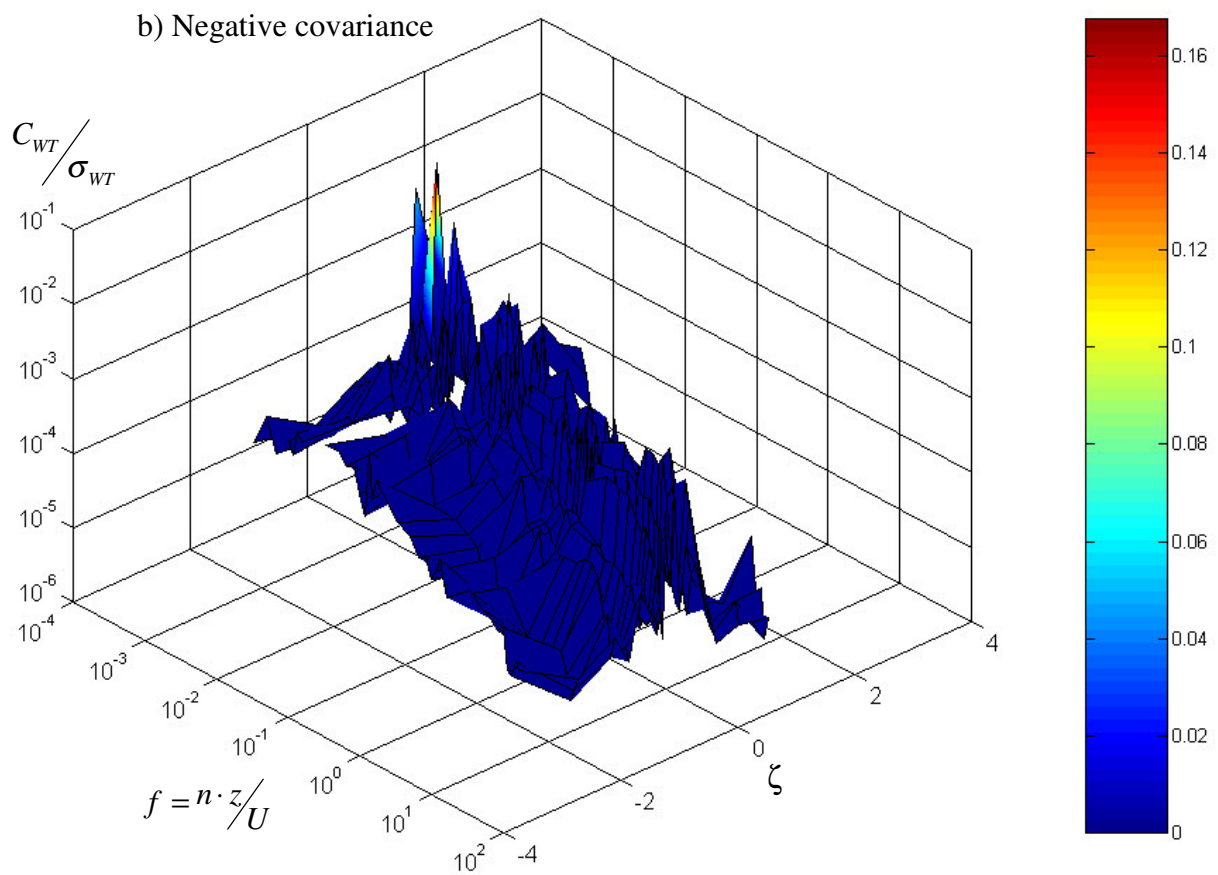
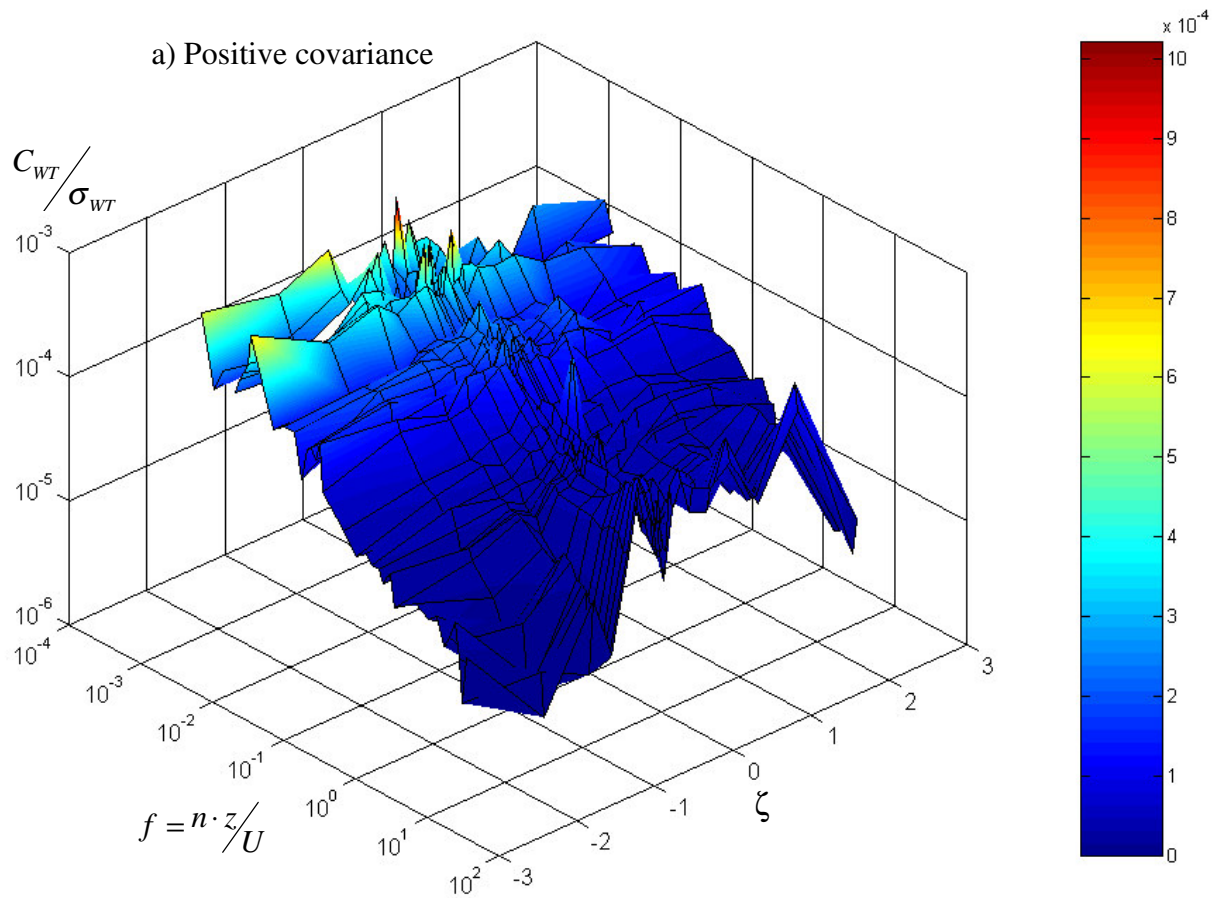


Figure 6. WT co-spectrum vs. stability parameter from the third urban measurement campaign (SASUA 3). a) Average of positive covariances. b) Average of negative covariances

However, in the case of C_{WT} , because of the definition of the stability parameter, the plot of positive co-variance shows upward heat flux in unstable conditions and downward heat flux in unstable conditions. The negative co-variance plot shows the opposite. Part (b) of figure 6 shows the negative portion of the co-spectrum. The most notable feature here is the lack of any downward heat transport in unstable conditions. This is expected simply from the definition of “unstable conditions” (chapter 2), however it is worth noting that sensible heat transport always has a bi-directional component in stable conditions. This is thought to be mainly because of the competition between nocturnal anthropogenic heat generation at the urban surface and radiative cooling. In conjunction with this result it is also noted that negative heat fluxes observed above the study city were never large in magnitude.

7.4.2 Fine Aerosol Flux

Figure 7 shows the co-spectrum of W and χ ($C_{W\chi}$). It is also split into separate “positive” and “negative” plots. Again, the positive part of the co-spectrum shown in 7 (a) is relatively uniform across the stability range. The Negative portion in 7 (b), however, behaves rather differently. A small counter gradient component of the flux exists across most of the stable range, as in figure 6 for sensible heat flux. However, the largest negative values are observed at low frequencies in the mildly unstable range.

This supports the discussion in chapter six of the reason for a depression in aerosol flux under unstable conditions, and the speculation on a possible source for downward moving particles. The conjecture was that a layer of elevated aerosol concentration may exist towards the top of the boundary layer, and downward movement of aerosol over the time periods indicated in figure 7 (b) would be expected if this were the case.

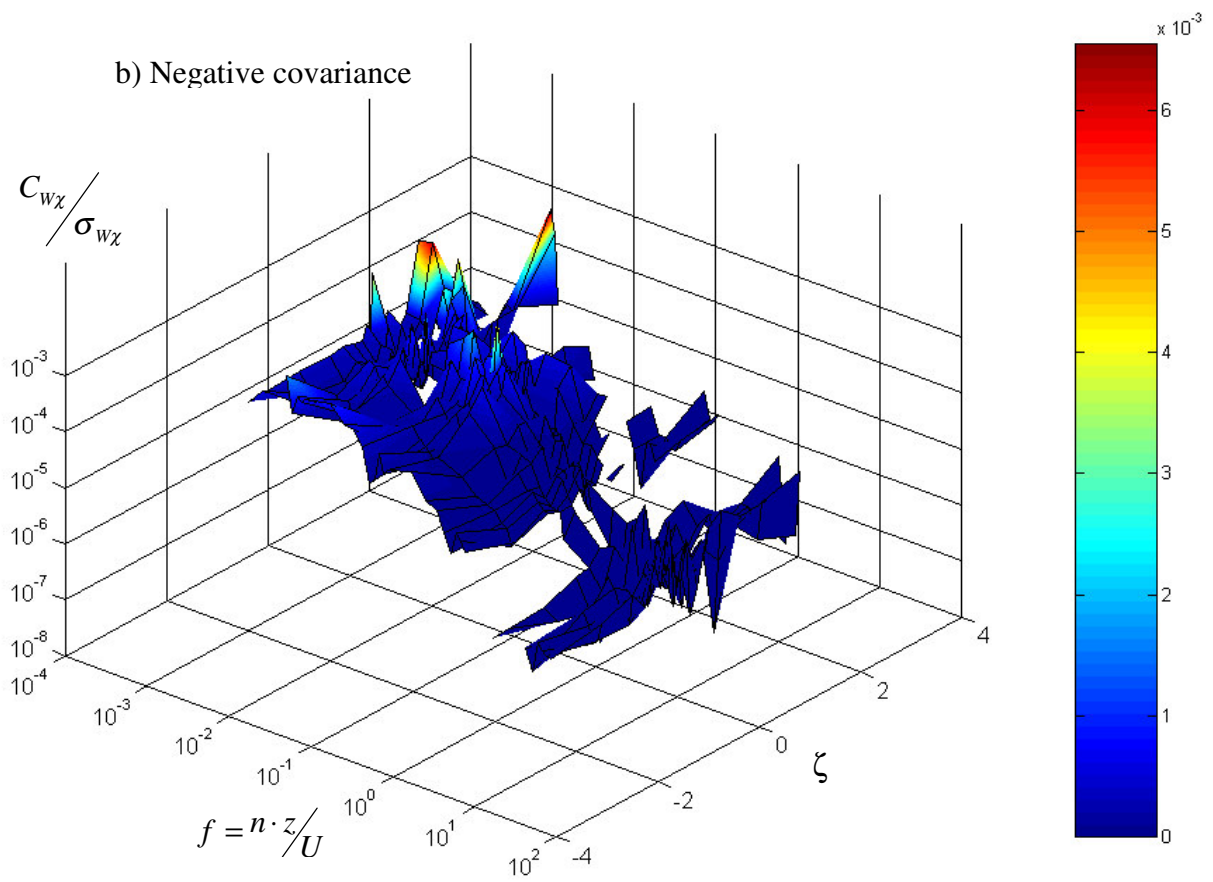
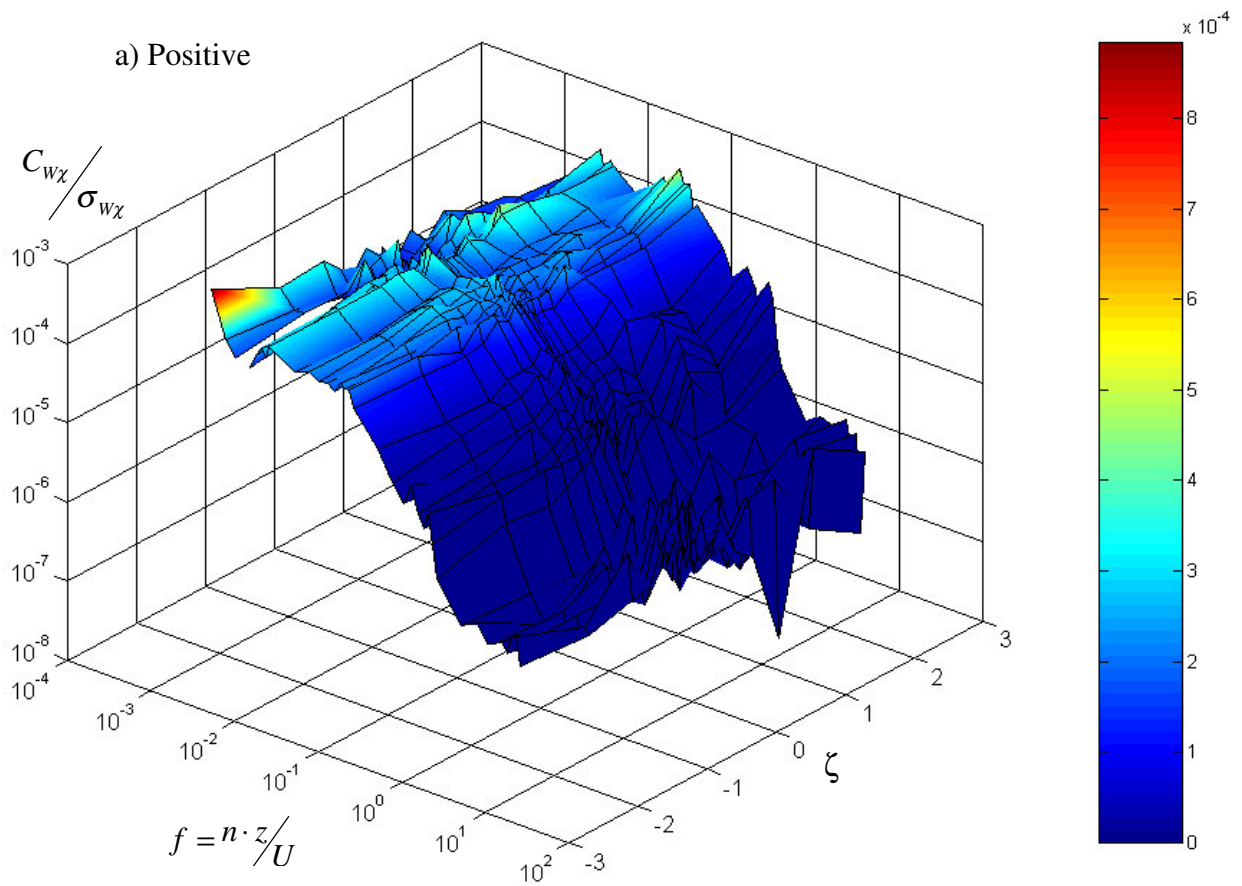


Figure 7. $W\chi$ co-spectrum vs. stability parameter from the third urban measurement campaign (SASUA 3). a) Average of positive covariances. b) Average of negative covariances

The final major point of interest in figure 7 is the fact that counter gradient aerosol transport (usually this means downward transport in the urban environment) appears to be restricted to relatively low frequencies at all stabilities, – the gaps in the plot at higher frequencies indicate that short period downward movements of aerosol were generally not observed. This conjecture will be revisited once more in the following section on probability density analysis of the heat and aerosol fluxes.

7.5 Probability Density Analysis

The concept of probability density analysis was introduced in chapter two. Here it is used as another means of understanding the coupling between vertical motions and entrained quantities. The virtual temperature and vertical wind speed probability density is examined first, followed by that for aerosol flux.

7.5.1 Temperature

Figure 8 shows the average joint probability density function for instantaneous fluctuations in air temperature and vertical wind speed. The two plots shown are constructed from the same data, but are differently presented in order to give an impression of the shape of the function. The individual values are the average frequencies of occurrence for the whole of the SASUA 3 campaign. Axes span a total of four times the variance of each time series.

The first point to note is the concentration of probability in the centre of the plot. This indicates that it is most common for both time series to remain close to their own mean values for most of the time. Large excursions of either the W or T time series are rare, and it appears that much of the sensible heat flux is transported by a large number of comparatively ‘low strength’ eddies. The other clear finding is that the probability density is very nearly circular. Although the city is a strong source of sensible heat on average, this is not obvious from inspection of figure 8.

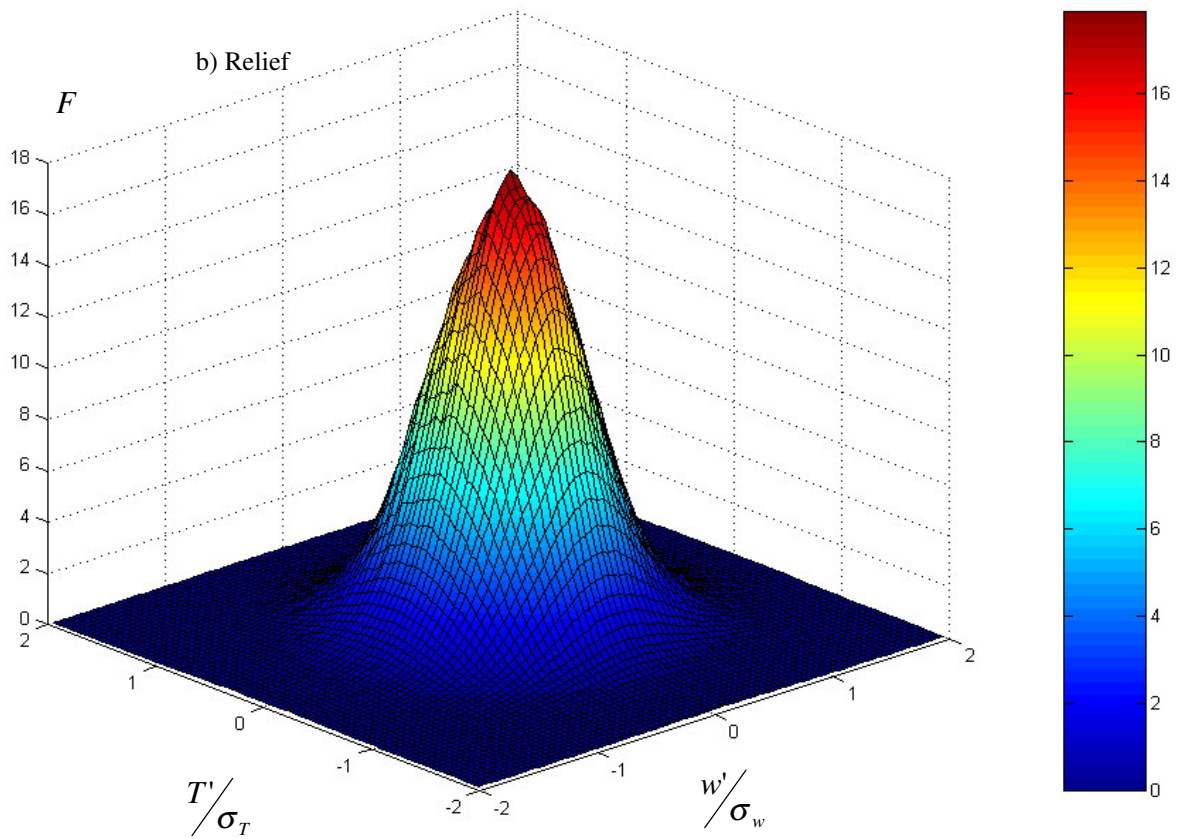
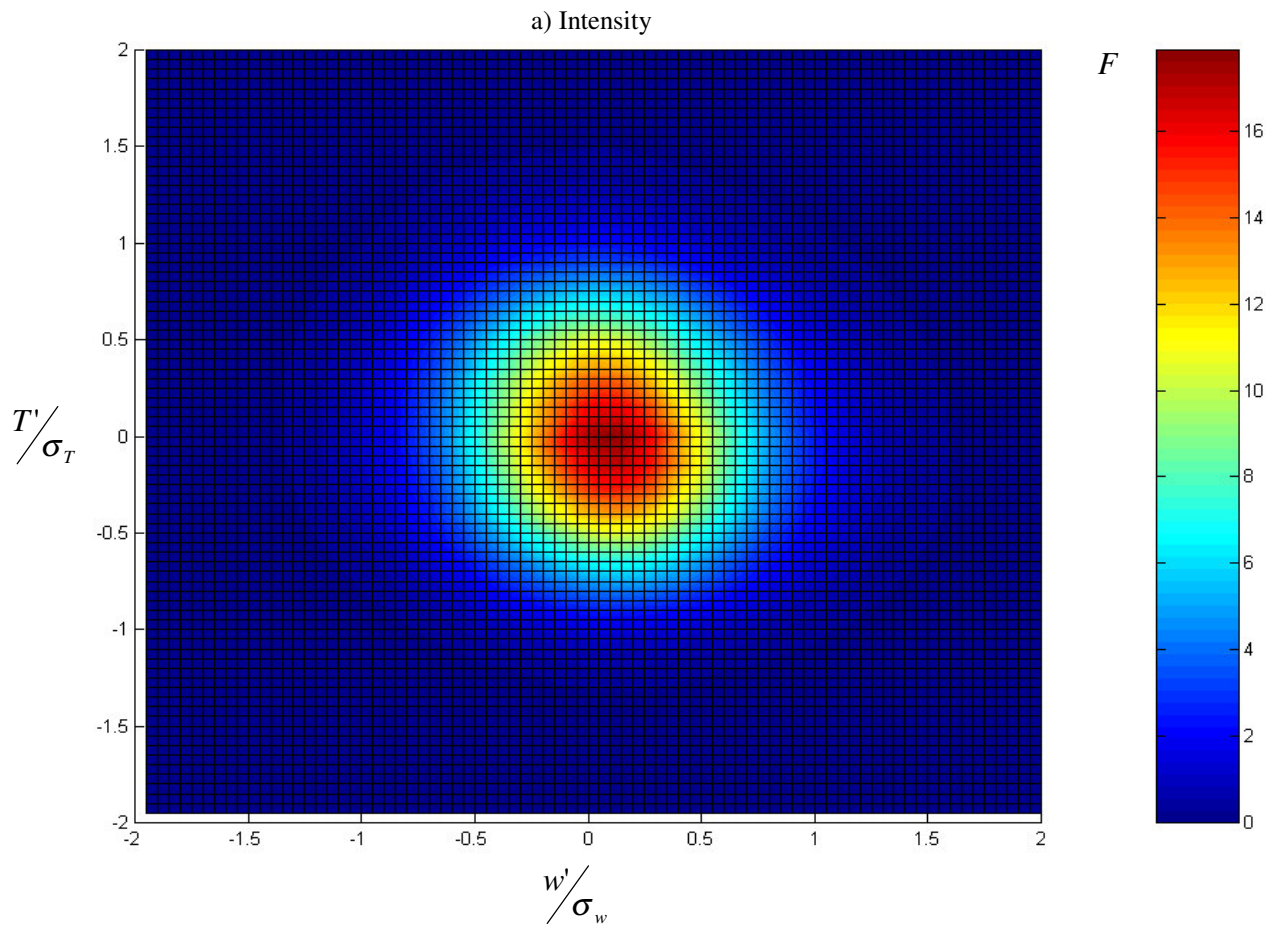


Figure 8. Joint probability density for turbulent fluctuations in vertical wind speed and air temperature. a) Intensity plot. b) Relief plot

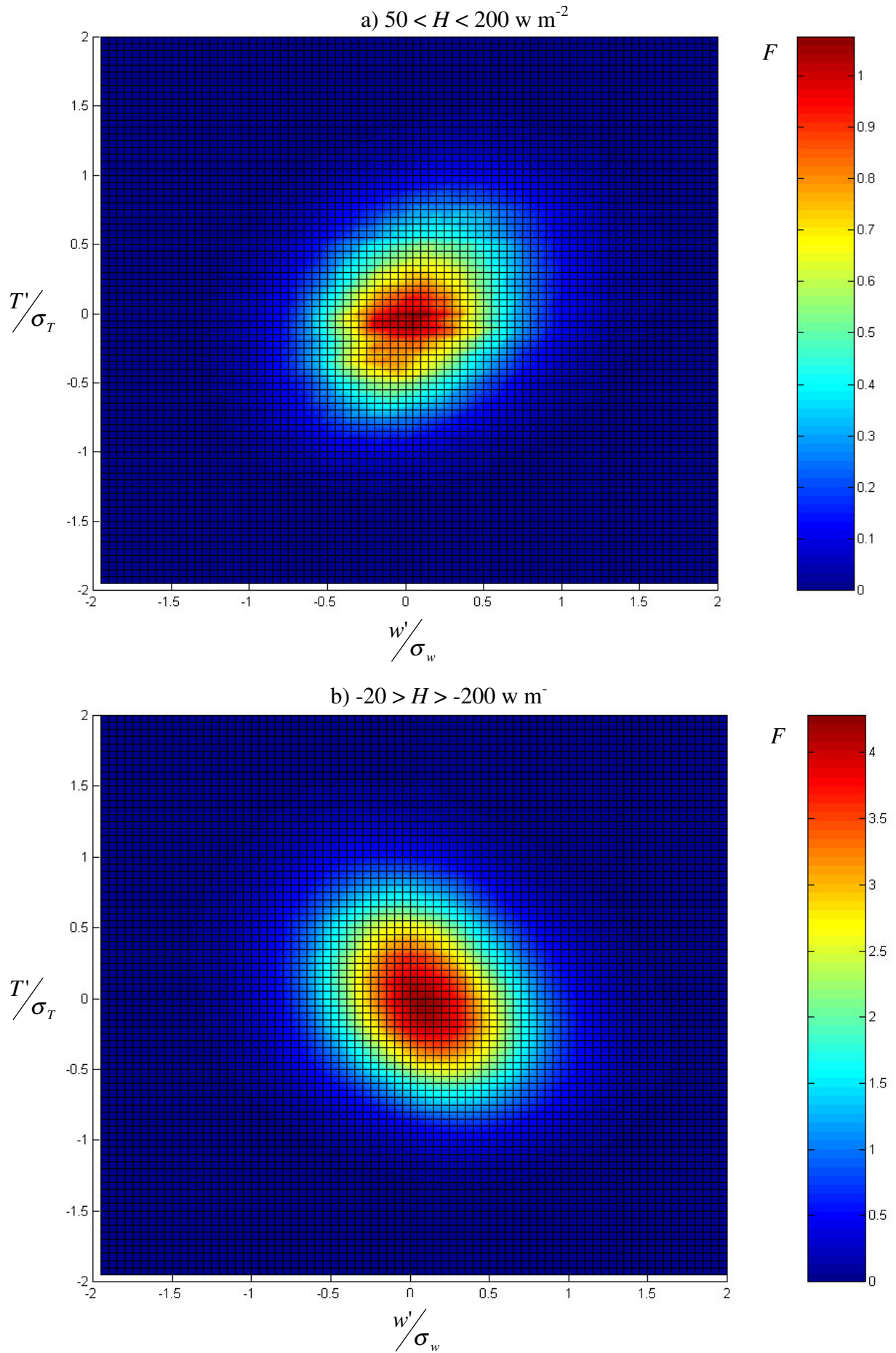


Figure 9. Joint probability density for turbulent fluctuations in vertical wind speed and air temperature. a) Positive sensible heat flux b) Negative heat flux

Figure 9 separates the sensible heat flux data to show the effect of the shape of the probability density on the measured flux. 9 (a) was constructed in a similar manner to figure 8, but all data included were taken from periods where the sensible heat flux was between $50 < H < 200 \text{ W m}^{-2}$. 9 (b) is similarly segregated for periods where the sensible heat flux was $-20 > H > -200 \text{ W m}^{-2}$.

The difference between the two plots in figure 9 is readily visible. Again, it emphasises the fact that the coupling between vertical wind speed and correlated entrained quantities is rather subtle. It shows the difference in appearance of the probability density where a flux is present. The noteworthy feature is that the distribution is still *nearly* circular and centred on the zero perturbation point. However, it has become slightly elliptical, with the long axis of the ellipse having a negative gradient in conditions of negative flux (again, chapter two contains an explanation of this). These probability densities will be used for comparison with those pertaining to aerosol flux.

7.5.2 Aerosol Concentration

Figure 10, similarly to figure 8 shows the average joint probability density for all data from SASUA 3. The shape of the distribution is qualitatively similar to that of figure 8, except that since the city is a strong aerosol source at most times, figure 10 (a) is perceptibly elliptical. The area of highest probability density is still located near the zero perturbation point of the plot ($w'/\sigma_w = 0, \chi'/\sigma_\chi = 0$). However, recalculating the distributions for mildly unstable periods (where for figure 11 (a), $1.5 < \zeta < 3$ and for figure 11 (b), $2 < \zeta < 3$) reveals slightly different behaviour.

Figure 11 shows the re-calculated data for the stability criteria given above. These conditions were chosen because it is during such conditions when the aerosol emission is apparently (and unexpectedly) suppressed (chapter six). In both cases the highest probability density has shifted away from (0,0), and there is even a suggestion that the distribution may be splitting into two separate maxima. Although it is difficult to see the

effect of this on the fluxes from the probability density analysis alone, it may be indicative of more complex behaviour than simple transport away from a single source.

The tentative finding that the average joint probability density function for aerosol flux behaves differently in stable and unstable conditions, and that it is dissimilar to that for sensible heat flux, supports the interpretation of the co-spectra above. It is not possible to ascertain from the probability analysis alone whether the unstable aerosol flux behaviour is caused by two separate aerosol sources, or by two distinct transport mechanisms. It is only *clear* that the instantaneous exchange velocity for aerosol is not a simple function of the variance of vertical wind speed and aerosol concentration.

However, in conjunction with the arguments set out in the context of the co-spectral analyses it is strongly suggestive of the former, and at least of complicating factors in the aerosol flux. Further data are required to gain a more reliable picture of the mechanism of aerosol transport in the unstable regimen, however it appears that aerosol transport is not entirely analogous to sensible heat transport under the conditions discussed.

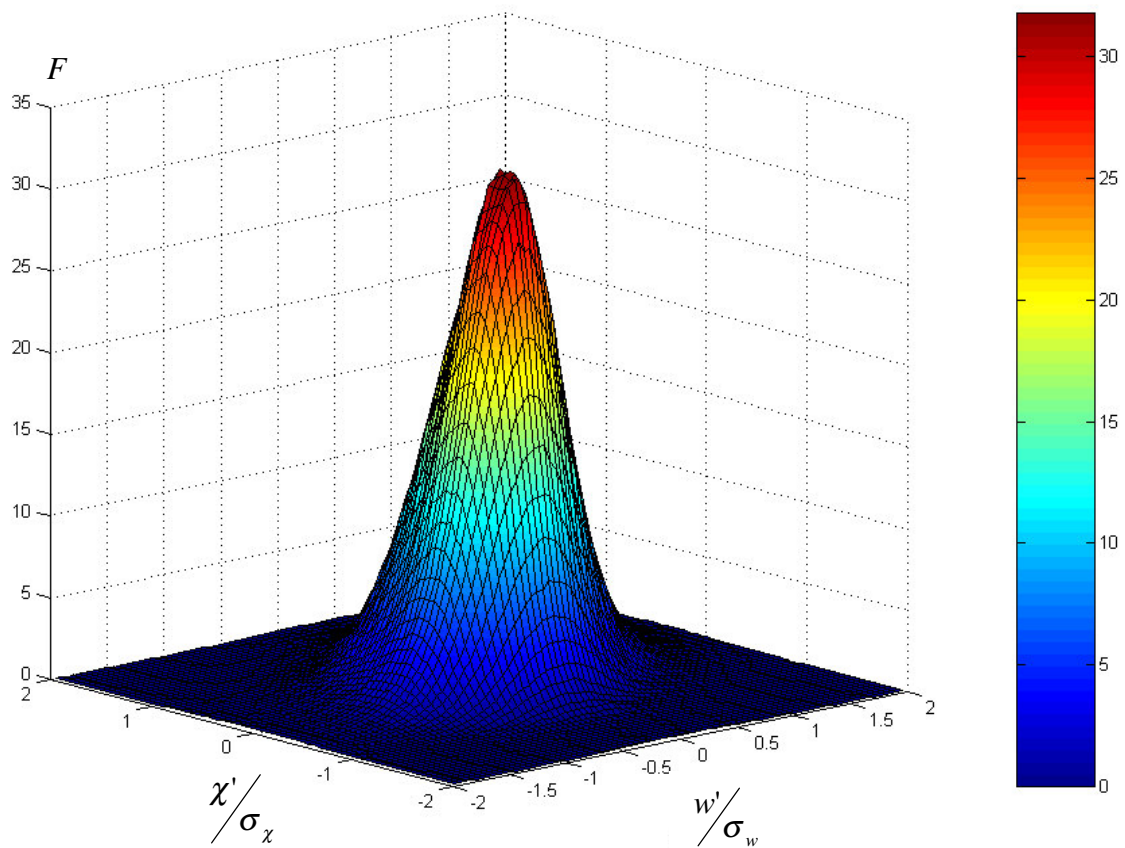
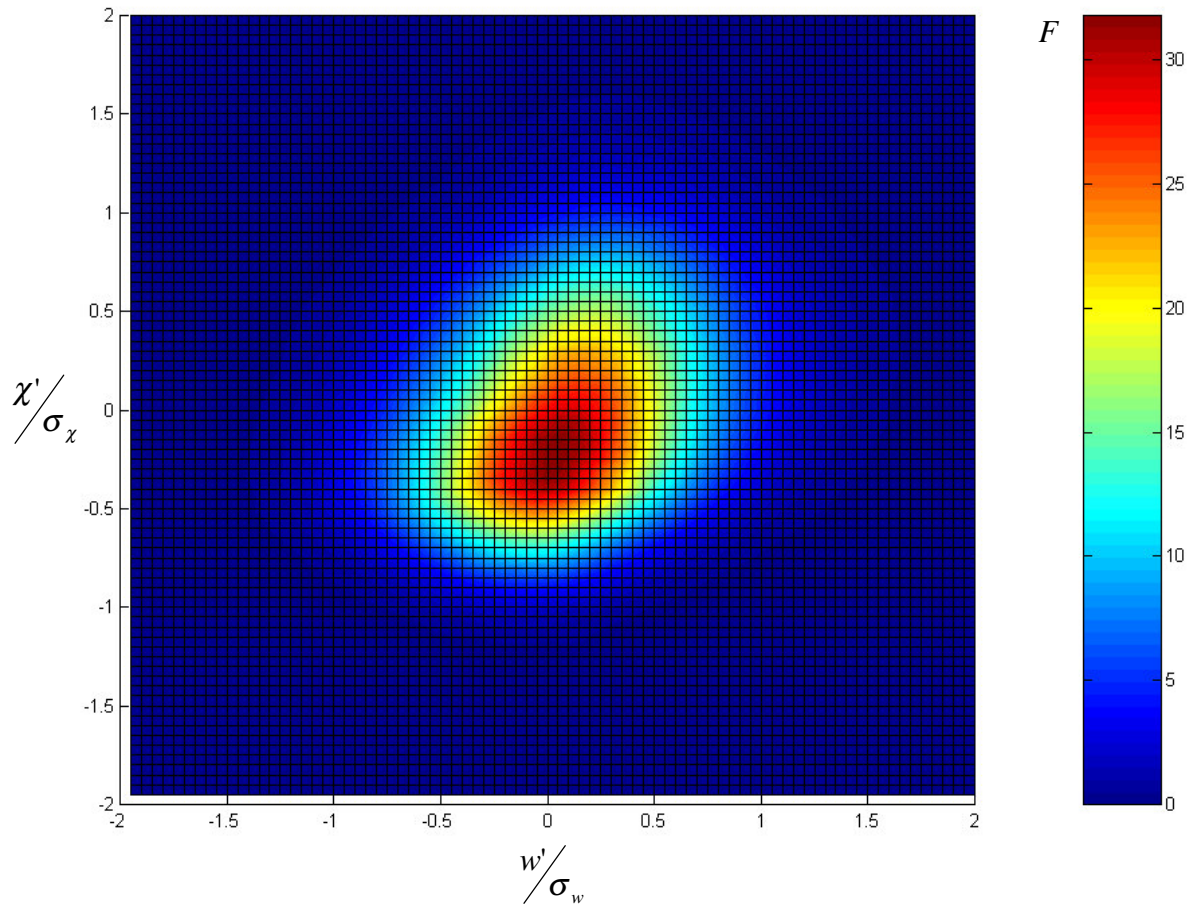


Figure 10. Joint probability density for turbulent fluctuations in vertical wind speed and aerosol concentration. a) Intensity plot. b) Relief plot

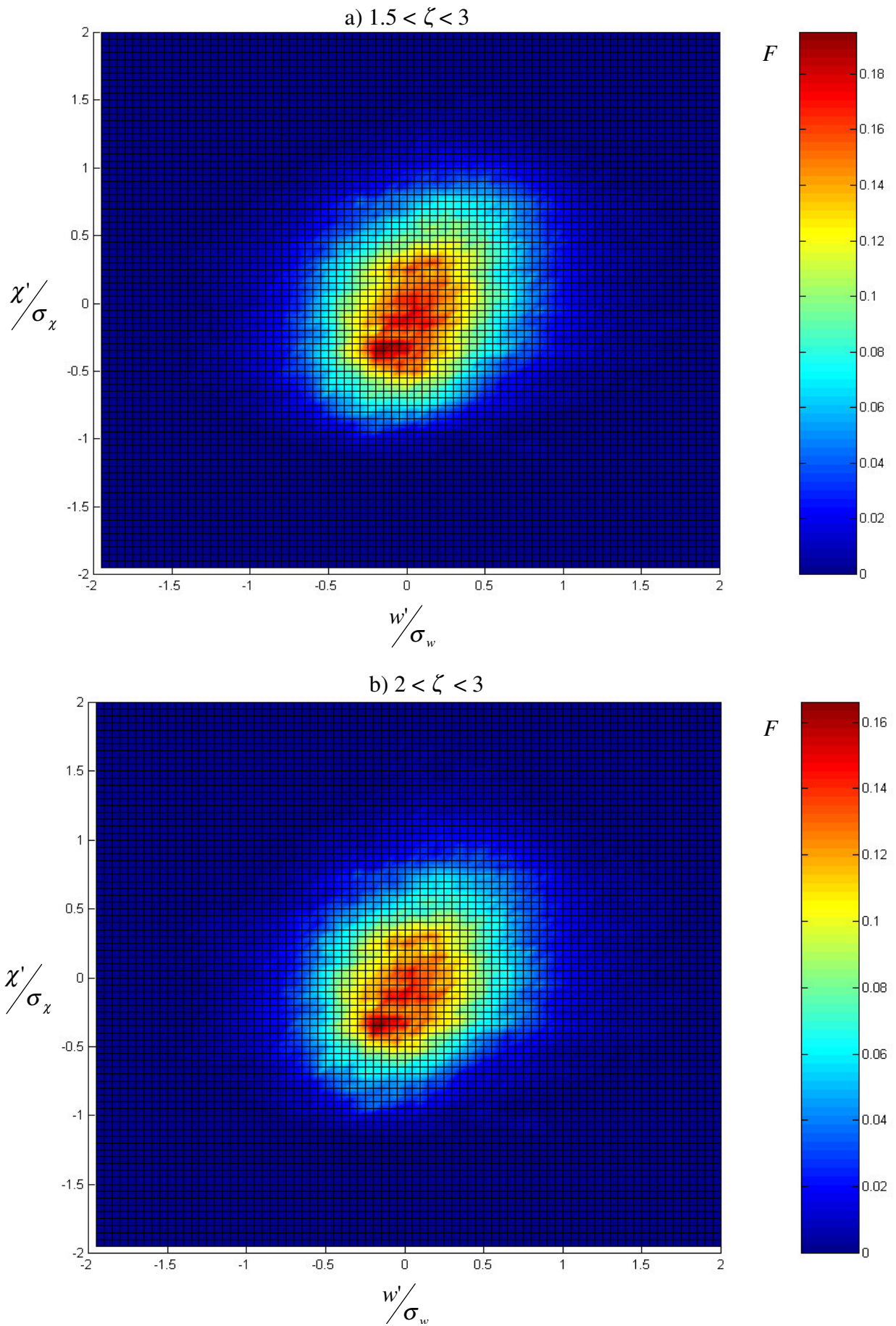


Figure 11. Joint probability density for turbulent fluctuations in vertical wind speed and aerosol concentration. Project averages over two mildly unstable ranges.

7.6 Summary

The energy balance for an urban area has been examined, with special reference to anthropogenic energy input. It is shown that the non-radiative heating of the urban surface examined is equivalent to the addition of 44 W m^{-2} to the system. Of this additional energy, which is assumed to be anthropogenic in origin, it has been estimated that around 30% is derived from fossil fuel combustion within the city. Possible sources for the remaining 60% include space heating and other electrically powered activities, for which the associated fossil fuel combustion takes place well outside the city.

The spectral and co-spectral behaviour of sensible heat and aerosol transport have been discussed. The stability dependence of the bi-directionality of sensible heat fluxes has been noted. Similarly, there is a stability dependence for downward aerosol flux, with strong low frequency downward transport of aerosol observed during unstable conditions.

The analysis of the probability density functions for vertical wind speed with virtual temperature and aerosol concentration shows evidence of complicating factors in the aerosol flux not present in the heat fluxes. A comparison of the probability density and co-spectral analyses for aerosol flux is suggestive of downward transport of aerosol from aloft competing with upward transport from urban surface sources, as suggested in chapter six. This requires further investigation, probably involving the gathering of more data, again under a wide variety of atmospheric conditions.